FINITE ELEMENT ANALYSIS OF FLOW, HEAT TRANSFER, AND FREE INTERFACES IN AN ELECTRON-BEAM VAPORIZATION SYSTEM FOR METALS

K.W. WESTERBERG[a], M.A. McCLELLAND[a,*] AND B.A. FINLAYSON[b]

[a] *Lawrence Livermore National Laboratory*, *PO Box 808*, *L-460*, *Livermore*, *CA 94550*, *USA*
[b] *Department of Chemical Engineering*, *Box 351750 University of Washington*, *Seattle*, *WA 98195-1750*, *USA*

SUMMARY

A numerical analysis is made of the liquid flow and energy transport in a system to evaporate metals. The energy from an electron-beam heats an axisymmetric metal disk supported by a water-cooled platform. Metal evaporates from the surface of a hot pool of liquid which is surrounded by a shell of its own solid. Flow in the pool is strongly driven by temperature-induced buoyancy and capillary forces, and is located in the transition region between laminar and turbulent flow. The evaporation rate is strongly influenced by the locations of the free boundaries. A modified finite element method is used to calculate the steady state flow and temperature fields coupled with the interface locations. The mesh is structured with spines that stretch and pivot as the interfaces move. The discretized equations are arranged in an 'arrow' matrix and are solved using the Newton–Raphson method. The electron-beam power and platform contact resistance are varied for cases involving the evaporation of aluminum. The results reveal the interaction of liquid flow, heat transfer and free interfaces. © 1998 John Wiley & Sons, Ltd.

KEY WORDS: liquid flow; energy transport; electron-beam

1. INTRODUCTION

In recent years, electron-beam (e-beam) technology has become increasingly important in metal processing operations. These systems can provide a high performance product with a reduced impact on the environment. They have the capability to provide high energy fluxes in an atmosphere which is relatively free of contaminants. These features allow the high evaporation rates required for the commercial vapor deposition and isotope separation of refractory metals. They are also of benefit in welding, refining, and casting operations. An improved understanding of transport processes would yield improvements in throughput, control, and system lifetime.

In a typical e-beam evaporator for metals, a melt confined by a water-cooled container is heated with energy from an electron-beam [1,2] (see Figure 1). The electron-beam is guided by a magnetic field to the target in high vacuum. A small fraction of the energy provides the heat necessary to evaporate the metal and another portion is lost due to thermal radiation and to the formation of 'skip' electrons. The remaining energy is transported by convection and conduction to the cooled container.

---

* Correspondence to: Lawrence Livermore National Laboratory, PO Box 808, L-460, Livermore, CA 94550, USA.

The metal evaporates from the surface of a pool of circulating liquid which is bound by a skull of its own solid. Flow is driven by thermally-induced gradients in the density (buoyancy effect) and surface tension (Marangoni effect). The flow intensity is high due to the low viscosities of metals and the large temperature gradients that are present in the system.

The effects of flow intensity have been investigated for buoyancy and capillary-driven flow in shallow rectangular cavities with differentially-heated side walls. In the more careful studies the critical flow intensity has been determined for steady state solutions which become unstable to small disturbances. In a recent study by McClelland [3] time-dependent simulations were performed at flow intensities as high as those observed in e-beam vaporizer pools. These results were extended to include a deformable free surface and Marangoni effects [4].

Detailed modeling of this system is also a challenge due to the presence of three interfaces joined at a 'trijunction' (see Figure 1). The locations of these interfaces separating solid, liquid and vapor phases are coupled to the liquid flow and energy transport in the vaporizer. Metal-casting, welding, and crystal-growth systems also share these features.

In an early numerical study of e-beam evaporation, Kheshgi and Gresho [5] estimated the locations of the pool boundaries and calculated the time-dependent flow and temperature fields. Although the study benefited from a very efficient computational procedure, the flow and heat transfer problem was decoupled from the interface locations.

A small number of investigators have analyzed systems with multiple free boundaries joined at a trijunction. In a study of laser irradiation, Służalec [6] used an enthalpy method for a case with a flat interface and no surface tension. Time-dependent calculations were done for tungsten and copper, using a high-power pulsed laser beam heat source. Two convection cells were formed in the pool, one above the other. Zacharia *et al.* [7] developed the method of discrete element analysis on fixed grids to calculate time-dependent flow and temperature fields, and locations for the liquid–gas interface and mushy zone. In their studies of two- and three-dimensional welding systems, Zacharia *et al.* [7–9] employed upwind differencing, often with coarse grids. Although the intense flows ($Re \sim O \ (10^2 – 10^4)$) were not fully resolved, favorable comparisons were achieved between calculated and measured surface temperatures and mushy zone locations. Ravindran *et al.* [10] analyzed laser surface melting using a mushy zone between the fluid and solid. Marangoni effects were included for a flat interface. The no-slip condition was applied at the liquid–mush interface by setting the velocity to zero in the
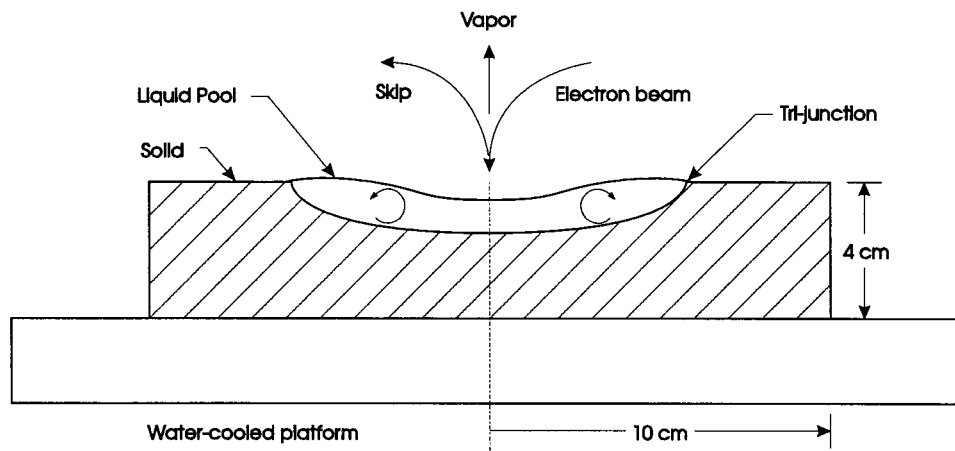
Figure 1. Evaporation of aluminum from a plate on a water-cooled platform.

mushy zone or solid. However, the authors do not indicate the conditions for elements which contain both the fluid and the mushy zone. Viscosities of 0.006 Pa-s are used, but only at a lower laser power of 0.25 kW.

In studies of the Czochralski crystal growth system, Brown and co-workers [11,12] employed the finite element method with a deforming mesh to track both solid–liquid and liquid–gas interfaces along with the trijunction. Using this method, specified nodes remained at interfaces and the interior nodes moved along vertical spines, following the approach described by Kistler and Scriven [13].

Tsai and Kou [14] employed a control volume-finite difference method to analyze flow and heat transfer in a steady state, two-dimensional welding system. The mesh deformed to track the liquid–gas interface, and a mushy zone approach was employed for the solid–liquid region. In a study of a floating zone crystal growth system, this approach was extended to provide for the tracking of both the liquid–gas and solid–liquid interface along with a trijunction [15]. In a later investigation the transport of a second species was included [16].

In previous studies by the authors [17–19] a two-dimensional planar model for the steady state e-beam evaporation from an aluminum melt was developed. Rotating spines were employed in a finite element method to track the horizontal position of the trijunction and the locations of the solid–liquid and liquid–vapor interfaces. The non-linear equations governing the flow field, temperature field and free boundary location were solved in a coupled manner using a Newton–Raphson method. In the first two studies [17,18] the vaporization rates were limited to low values. Later [19] the material inventory constraints were improved, allowing high evaporation rates to be achieved. In these studies the electron-beam power and width were varied along with the viscosity and Marangoni contribution. The results show the strong influence of deformable free boundaries on e-beam evaporation.

In this investigation, we employ the same finite element method to analyze the e-beam evaporation of aluminum from an axisymmetric plate (see Figure 1). The flow and temperature fields, along with the free boundary locations, show the effects of variations in the e-beam power and contact resistance.

2. MODEL EQUATIONS

2.1. Field equations

In this model of e-beam evaporation, the influence of the vapor phase is included through the application of boundary conditions at the top surface of the melt, as described in Section 2.2. In a more detailed description, the field equations for the vapor phase would be solved simultaneously with the equations for the liquid and solid phases.

Liquid flow in the pool is governed by the steady state continuity and momentum equations for a Newtonian liquid:

$$\nabla \cdot \underline{u} = 0, \tag{1}$$

$$\rho_0 \underline{u} \cdot \nabla \underline{u} = -\nabla p + \mu \nabla^2 \underline{u} + \rho_0 \underline{g}[1 - \beta(T - T_0)], \tag{2}$$

where $\underline{u}$ is the velocity, p is the pressure and T is the temperature. The reference density, ρ_0, viscosity, μ, and volumetric coefficient of expansion, β, are taken to be uniform in the liquid pool. In applying the Boussinesq approximation the liquid density is varied linearly about the melting point value in the body force term only.

In the absence of compressive work and viscous dissipation, the energy equation takes the following form:

$$\rho_0 C_p \underline{u} \cdot \nabla T = k \nabla^2 T. \tag{3}$$

The heat capacity at constant pressure, C_p, and thermal conductivity, k, are taken to be uniform within a given phase. In the solid phase there is no flow and the left-hand-side of Equation (3) vanishes.

The Reynolds and Peclet numbers provide measures of the flow intensity and thermal convection, respectively:

$$Re = \frac{\rho_0 u_{max} d_{pool}}{\mu} \qquad Pe = \frac{u_{max} d_{pool}}{\alpha}.$$

The characteristic length in the above expression is the depth of the liquid pool at the symmetry axis, d_{pool}. The maximum surface speed, u_{max}, is the characteristic velocity.

2.2. Material inventory constraints and boundary conditions

2.2.1. Mass inventory and phase distribution. Two constraints are applied for the inventory of solid and liquid material in the system. The first condition is a specification for the average level of material in the system, $\bar{h}_0$:

$$\bar{h}_{ls} \equiv \frac{2 \int_0^{r_{disk}} hr \, dr}{r_{disk}^2} = \bar{h}_0. \tag{4}$$

Here r_{disk} is the radius of the disk (see Figure 1). The second condition is that the solid–vapor interface has a uniform elevation:

$$h = h_s \quad \text{for} \quad r_{tri} \leq r \leq r_{disk}, \tag{5}$$

where r_{tri} is the radial co-ordinate of the trijunction. With the assumption of uniform material density throughout the disk, these two conditions specify the mass of the disk. The combination of Equations (4) and (5) yields a relationship for the average level of liquid in the pool:

$$\bar{h}_l = \frac{r_{disk}^2 \bar{h}_{ls} - (r_{disk}^2 - r_{tri}^2) h_s}{r_{tri}^2}. \tag{6}$$

In an alternative formulation, $\bar{h}_l$ and h_s could be specified, and $\bar{h}_{ls}$ would be a function of these two elevations according to Equation (6).

In using the material inventory constraints (Equations (4) and (5)), there are limits to the difference that can be applied to the levels $\bar{h}_0$ and h_s. For metal flow systems, surface tension forces balance the variations in the surface hydrostatic pressure associated with liquid level changes. These forces balance over a capillary length scale $L_c = (\sigma/\rho_0 g)^{1/2}$ in which σ is the surface tension. Stable numerical solutions are not available for liquid level changes significantly larger than L_c. Thus, the approximate constraint

$$|\bar{h}_l - \bar{h}_s| < O(L_c) \tag{7}$$

is employed with Equations (4) and (5).

In earlier papers [17,18] a mass inventory constraint of the type given by Equation (4) was not used, resulting in a 'natural' pool level which was determined by the mechanics of flow. In a later work [19] the use of a mass inventory constraint provided a much better model because the pool level was varied as it is in practice.

2.2.2. Flow boundary conditions. For the specification of steady state flow conditions at the pool boundaries, it is assumed that the evaporation and make-up feed rates are small and have a negligible kinematic effect on the flow field. All pool boundaries are then material boundaries, and the interfacial flow obeys the steady state kinematic equation:

$$\underline{n} \cdot \underline{u} = 0 \quad \text{at} \quad \underline{x} = \underline{x}_{lv}, \tag{8}$$

where $\underline{n}$ is an outward pointing surface normal vector. In addition to Equation (8), the shear stress vanishes at the symmetry axis:

$$\underline{n} \cdot \underline{\underline{\tau}} \cdot \underline{t} = 0 \quad \text{at} \quad r = 0 \tag{9}$$

and the tangential velocity is zero at the solid–liquid interface:

$$\underline{t} \cdot \underline{u} = 0 \quad \text{at} \quad \underline{x} = \underline{x}_{sl}. \tag{10}$$

A force balance at the liquid–vapor interface gives

$$\underline{M} \equiv \underline{n} \cdot (p\underline{\underline{\delta}} + \underline{\underline{\tau}}) + \sigma \left(\frac{\mathrm{d}\underline{t}}{\mathrm{d}s} + \frac{\mathrm{d}\underline{t}_1}{\mathrm{d}s_1} \right) + \frac{\mathrm{d}\sigma}{\mathrm{d}T} \frac{\mathrm{d}T}{\mathrm{d}s} \underline{t} - \underline{n}\pi_v = 0. \tag{11}$$

The pressure and viscous contributions for the liquid are included in the first term of Equation (11). The second term is the normal stress resulting from surface tension and interface curvature, in which there are contributions in and out of the r–z calculation domain. For the r–z plane, $\underline{t}$ is the surface tangent vector and s is the surface arc length. The vector $\underline{t}_1$ and co-ordinate s_1 are used in a plane which includes the surface normal vector and a vector normal to the r–z plane. In this normal stress term, the surface tension, σ, is taken to be constant at its melting point value. The third term accounts for the Marangoni effect, in which a surface shear stress is generated by temperature gradients in the surface tension. The final term in Equation (11) is the normal stress generated by the thrust of the departing vapor. The vapor thrust of the vaporization of ideal atoms at low rates is approximated by

$$\pi_v = \frac{p_{vap}(T)}{2}, \tag{12}$$

in which p_{vap} is the equilibrium vapor pressure [20]. Since Equation (11) includes surface tension, two endpoint conditions are required. At the symmetry axis, the interface is horizontal:

$$\underline{n} = \underline{\delta}_z \quad \text{at} \quad r = 0. \tag{13}$$

The other endpoint is a trijunction where vapor, liquid and solid phases meet. We take this junction to be located at a sharp edge with specified elevation h_s (see Equation (5)).

2.2.3. Thermal boundary conditions. At the liquid–vapor interface an energy balance accounts for the power provided by the electron-beam and the energy losses due to evaporation and thermal radiation.

$$\underline{n} \cdot \underline{q} = (-\underline{n} \cdot \underline{\delta}_z)q_b + q_v + q_r. \tag{14}$$

The absorbed energy flux from the electron-beam is assumed to follow a Gaussian distribution of radius σ_b centered on the axis of symmetry:

$$q_b = \frac{\gamma Q_b}{2\pi\sigma_b^2} \mathrm{e}^{-r^2/2\sigma_b^2}. \tag{15}$$

The beam is taken to be sufficiently narrow, so that essentially all of the electron-beam power, Q_b, is incident on the pool. The fraction of e-beam energy absorbed by the pool, γ, is taken to be uniform and independent of the angle of incidence. The coefficient of the first term on the right-hand-side of Equation (14) accounts for the influence of surface deformation on the normal component of heat flux. The evaporation energy loss includes kinetic energy and latent heat contributions:

$$q_v = n_v \left(\frac{2RT}{M} + \Delta H_{vap} \right). \tag{16}$$

For low evaporation rates, the vapor mass flux, n_v, is approximated by the Langmuir expression:

$$n_v = p_{vap}(T) \left(\frac{M}{2\pi RT} \right)^{1/2}. \tag{17}$$

The heat flux resulting from radiant heat exchange with the surroundings is given by

$$q_r = \varepsilon(T)\sigma_{SB}(T^4 - T_\infty^4), \tag{18}$$

where ε is the emissivity and T_∞ is the temperature of the surroundings.

For steady state conditions, the temperature at the solid–liquid interface is the melting point value:

$$T = T_{mp} \quad \text{at} \quad \underline{x} = \underline{x}_{sl}. \tag{19}$$

An energy balance at the solid–liquid interface yields

$$\underline{n} \cdot (k\nabla T)\big|_l = \underline{n} \cdot (k\nabla T)\big|_s, \tag{20}$$

and the normal heat flux disappears at the axis of symmetry:

$$\underline{n} \cdot \underline{q} = 0. \tag{21}$$

For metals with low melting point temperatures, this expression is also applied at solid–vapor boundaries, because the contribution of thermal radiation is small. Newton's law of cooling is used to describe the transfer of energy between the solid metal and the platform cooling water with temperature T_w.

$$\underline{n} \cdot \underline{q} = h_{pl}(T - T_w). \tag{22}$$

The heat transfer coefficient, h_{pl} is taken to be uniform, and it includes the resistance due to disk–platform contact, solid conduction in the platform, and energy transport in the water.

3. FINITE ELEMENT METHOD

3.1. Mesh parameterization

Deforming meshes structured with spines [13] are used to track the liquid–vapor and solid–liquid interfaces (see Figure 2). Specified nodes remain on interfaces while interior nodes move along these spines. In order to treat the solid–liquid interface which moves horizontally at the trijunction and vertically at the symmetry axis, we employ spines that emanate from a single 'anchor' point above the liquid–vapor interface at the symmetry axis. Each spine intersects the top surface of the metal disk before continuing to base points distributed along the side and lower surfaces of the disk.
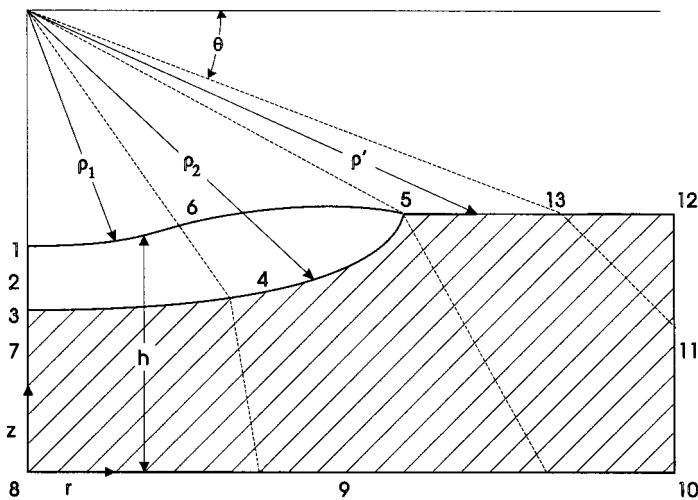
Figure 2. Mesh variables, spines ($\cdots$) and interfacial segments and endpoints. The interfacial variables and associated conditions are given in Table I.

For each spine passing through the liquid, there are three variables (see Figure 2). The length co-ordinates ρ_1 and ρ_2 are the respective distances from the anchor point to the liquid–vapor and liquid–solid interfaces. There is also a pivot angle, θ, to accommodate the horizontal motion of the trijunction. For a spine passing only through the solid, a single length co-ordinate, ρ', is used with the pivot angle. A spine is completely defined with these co-ordinates, and the anchor and base locations.

Several expressions are used to insure that the mesh deforms smoothly. First, the relative spacing of the nodes is preserved along a spine within a given phase. Second, the angular deformation of the mesh is oriented about the motion of the trijunction spine. For the kth spine intersecting the liquid–vapor interface, the following condition

$$\cot \theta_{\text{tri}} - c_k \cot \theta_k = 0 \tag{23}$$

preserves the relative spacing of the spines along a horizontal line above the interface. Here c_k are constant coefficients. For the spines passing through the top solid–vapor interface, the condition

$$\cot \theta_k - \cot \theta_{tri} - c'_k (\cot \theta_w - \cot \theta_{\text{tri}}) = 0 \tag{24}$$

serves the same purpose. The elevation of the trijunction and solid–vapor interface is held constant according to Equation (5):

$$\rho'_k \sin \theta_k - h_s = 0. \tag{25}$$

This constraint is also applied to the liquid–vapor interface during start-up calculations.

3.2. Discretization

The field Equations (1)–(3) and boundary conditions are discretized using the Galerkin finite element method [21,22]. The velocities, temperatures and co-ordinate mapping are represented by two-dimensional quadratic basis functions, and the pressure is represented by linear basis functions. The weak forms of the momentum and energy equations, in which the interfacial stress and heat flux conditions are incorporated as natural boundary conditions, are used.

The discretized versions of the field Equations (1)–(3) are applied at interior locations in the usual manner, but the treatment of boundary conditions is more complex. Table I lists the boundary conditions and associated variables for the interfacial endpoints and interior segments shown in Figure 2. Attention is given to conditions at endpoints and 'distinguished' conditions which are associated with the determination of free boundary variables.

At the symmetry axis node on the top surface (endpoint no. 1) the flow is stagnant ($\underline{u} = 0$), and the symmetry condition in Equation (13) for the liquid–vapor interface is applied in its natural form [13]:

$$\underline{n} \cdot \underline{M} = 0 \quad \text{at} \quad r = 0, \tag{26}$$

where $\underline{M}$ is the force balance, given in Equation (11), at the liquid–vapor interface. This condition is distinguished because it is applied for the determination of ρ_1. For convenience in assembling the solution matrices, Equation (26) and the condition $u_z = 0$ are switched with respect to their associated variables.

At the trijunction (endpoint no. 5) the continuity equation is replaced by the liquid level condition in Equation (4). In effect, the liquid pressure at this location is adjusted so that a specified level of material is maintained in the melt.

The liquid level condition (Equation (4)) at endpoint no. 5, could not be employed with the flow conditions at endpoint no. 1 in two of the earlier studies [17,18]. In these previous studies, Equation (11) was employed at endpoint no. 1 with the condition $\underline{t} = \underline{\delta}_r$. In addition, the kinematic condition (Equation (8)) was applied as the distinguished condition. This formulation was not used since the loss of a continuity equation (endpoint no. 5), combined with $\underline{u} \neq 0$ and high liquid pressures at endpoint no. 1, resulted in significant material leakage across the symmetry line [19].

At the solid–liquid interface (segment no. 4) and trijunction (endpoint no. 5) the melting point specification given in Equation (19) is applied as the distinguished condition for the

Table I. Interfacial conditions and variables for the segments and endpoints shown in Figure 2

Segment or endpoint	$\underline{u}$	p	T	θ	ρ_1	ρ_2	ρ'
1	u_r, M_z	c	q_{lv}, q_0	f	u_z	—	—
2	u_r, τ_{zr}	c	q_0	—	—	—	—
3	u_r, u_z	c	q_{sl}, q_0	—	—	T_{mp}	—
4	u_r, u_z	c	q_{sl}	—	—	T_{mp}	—
5	u_r, u_z	$\bar{h}_{ls}$	q_{sl}, q_{lv}	T_{mp}	—	—	h_s
6	$\underline{M}$	c	q_{lv}	$\theta_{tri,liq}$	u_n	—	—
7	—	—	q_0	—	—	—	—
8	—	—	q_0, q_{pl}	—	—	—	—
9	—	—	q_{pl}	—	—	—	—
10	—	—	q_0, q_{pl}	—	—	—	—
11	—	—	q_0	—	—	—	—
12	—	—	q_{pl}, q_0	f	—	—	f
13	—	—	q_0	$\theta_{tri,sol}$	—	—	h_s

Abbreviations: c, continuity, Equation (1); f, fixed variable; $\bar{h}_{ls}$, material level, Equation (4); h_s, solid level, Equation (25); $\underline{M}$, liquid–vapor momentum, Equation (11); M_z, surface normal condition, Equation (26); q_{lv}, liquid–vapor thermal, Equation (14); q_{sl}, solid–liquid thermal, Equation (20); q_{pl}, platform thermal, Equation (22); q_0, insulated boundary, Equation (21); T_{mp}, isotherm, Equation (19); u_n, kinematic, Equation (8); $u_r, u_r = 0$; $u_z, u_z = 0$; $\theta_{tri,liq}$, Equation (23); $\theta_{tri,sol}$, Equation (24); $\tau_{zr}, \tau_{zr} = 0$, Equation (9).

variables ρ_2 and the angular co-ordinate θ, respectively. At the liquid–vapor interface, the kinematic condition (Equation (8)) is the constraint associated with the variable ρ_1. All other conditions involve the distribution of elements or the conventional application of essential and natural boundary conditions.

3.3. Solution of residual equations

The non-linear algebraic equations representing the free-boundary problem take the form:

$$\underline{\mathscr{F}}(\underline{U}, \underline{\beta}) = \underline{0} \qquad \underline{\mathscr{G}}(\underline{U}, \underline{\beta}) = \underline{0}. \tag{27}$$

$\underline{\mathscr{F}}$ is a vector representing all of the residuals for the field equations (Equations (1)–(3)). The vector $\underline{\mathscr{G}}$ represents the residuals for the distinguished conditions used to calculate the free interface locations (Equations (8)–(19)), and the mesh conditions (Equations (23) and (25)). The vector $\underline{U}$ represents the velocity, pressure, and temperature variables and $\underline{\beta}$ represents the spine variables.

A Newton–Raphson method applied to Equation (27) yields the following matrix problem at each iteration:

$$
\begin{bmatrix}
\searrow & 0 & & | \\
\frac{\partial \mathcal{F}}{\partial \underline{U}^\dagger}\Big|^s & & \frac{\partial \mathcal{F}}{\partial \underline{\beta}^\dagger}\Big|^s \\
0 & \searrow & | \\
\text{---} \frac{\partial \mathcal{G}}{\partial \underline{U}^\dagger}\Big|^s \text{---} & \frac{\partial \mathcal{G}}{\partial \underline{\beta}^\dagger}\Big|^s
\end{bmatrix}
\begin{bmatrix}
\underline{U}^{s+1} \\
\\
\underline{\beta}^{s+1}
\end{bmatrix}
=
\begin{bmatrix}
-\mathcal{F}^s + \frac{\partial \mathcal{F}}{\partial \underline{U}^\dagger}\Big|^s \underline{U}^s + \frac{\partial \mathcal{F}}{\partial \underline{\beta}^\dagger}\Big|^s \underline{\beta}^s \\
\\
-\mathcal{G}^s + \frac{\partial \mathcal{G}}{\partial \underline{U}^\dagger}\Big|^s \underline{U}^s + \frac{\partial \mathcal{G}}{\partial \underline{\beta}^\dagger}\Big|^s \underline{\beta}^s
\end{bmatrix}
\tag{28}
$$

Here s is the iteration index. The form of the Jacobian is an 'arrow' matrix and an efficient solution algorithm is given elsewhere [23]. Gaussian elimination is performed on the $\partial \underline{\mathscr{F}}/\partial \underline{U}^\dagger$ sub-matrix and on a constructed dense matrix of size $NB \times NB$, where NB is the length of the $\underline{\beta}$ vector. The $\partial \underline{\mathscr{F}}/\partial \underline{U}^\dagger$ term is assembled and eliminated with the frontal method [24].

The arrow matrix formulation (Equation (28)) provides flexibility and efficiency. Given their differing structures, it is natural to separate the field equations from the distinguished and mesh conditions. One set of equations can be changed without disturbing the other. For example, moving mesh capabilities can be added to an existing finite element code without having to reformulate the field equations. The arrow matrix formulation provides computational efficiency by retaining a small bandwidth of the Jacobian matrix for the field equations and increasing it for a relatively small number of distinguished and mesh conditions. If the mesh constraints and field equations were combined for the metal evaporation system, the bandwidth would be considerably larger due to the material level constraint (Equation (4)) and the horizontal position of the trijunction, which is an explicit variable in most of the mesh conditions. Thus, the arrow matrix formulation provides considerable benefit for problems with moving boundaries and global constraints.

Table II. Parameters for aluminum inventory, electron-beam configuration, and cooling

$Q_b = 24-32$ (28) kW	$T_w = T_\infty = 25°C$
$\sigma_b = 0.008$ m	$\bar{h}_0 = \bar{h}_s = 0.04$ m
$h_{pl} = 2000-5000$ (4000) W m^{-2} K^{-1}	$r_{disk} = 0.1$ m

4. EVAPORATION RESULTS

Steady state calculations were performed for the evaporation of pure aluminum. The flows in physical e-beam evaporation pools are transient with flow intensities in the transition regime between laminar and turbulent flow. The steady state results of this study are taken to be representative of the time-averaged flows.

The majority of the physical properties are evaluated at the melting point temperature of 660°C and are taken to be uniform within a given material phase (see Appendix 1). However, the temperature dependence is included in the emissivity $\varepsilon(T)$, the vapor pressure $p_{vap}(T)$, the surface tension in the Marangoni term of Equation (11) and the liquid density in the body force term of Equation (2). It is the variation of the density and surface tension with temperature that drives the liquid flow in the pool. As discussed below the viscosity is 20-fold larger than the physical value.

Operating parameters for the evaporation system shown in Figure 1 are listed in Table II. The average level of material in the metal ingot is taken to be 0.04 m, the same value as the disk thickness. A range of values is considered for the electron-beam power and heat transfer coefficient for energy transport between the ingot and water-cooled platform. This range of values for h_{pl} overlaps the range given in a recent compilation of metal-mold interfacial coefficients [25].

In this study, results were first obtained for a 'base case'. (Base case values are denoted by '( )' when a range of values is given in Table II). As mentioned above, the base case viscosity is 20-fold greater than the physical value. At lower viscosity values, the flow is more intense and difficult to resolve. The search for steady state solutions is more difficult, making a parameter study less tractable.

In an earlier study on evaporation of aluminum from a crucible [18] the viscosity ratio $\mu^* = \mu/\mu_{meas}$ was varied from 1.25 to 20. For flows driven by buoyancy forces alone, a 16-fold decrease in μ^* resulted in a 42% decrease in evaporation rate. For liquid metal flows in e-beam evaporation pools the general circulation characteristics are the result of driving forces and inertial resistive forces, with viscosity playing a lesser role. As the viscosity decreased and the Reynolds number increased the details of the flow field changed significantly, but the overall changes in the thermal transport characteristics were relatively small. Thus, results for the base case ($\mu^* = 20$) should provide relevant insight despite the artificially high viscosity.

4.1. Base case

Calculations were made on a coarse grid M1 with 5255 unknowns and a fine mesh M2 with 11 543 unknowns. A deformed fine mesh for the base case is shown in Figure 3(a). The elements are concentrated near the pool boundaries where the gradients are largest. The spines originate from an anchor point, 0.03 m ($z = 0.07$ m), above the solid–vapor interface on the symmetry axis ($r = 0$).

There is a depression in the vicinity of the beam impact area formed by the thrust of the departing vapor. Outside this area, owing to the material inventory constraint (Equation (4)), the level of the liquid surface is higher than the top surface of the solid.

In the right half of the pool, the liquid circulates in a clockwise direction within a single cell (see Figure 3(c)). The streamlines and temperature contours are smooth, indicating that the flow field is well resolved (see Figure 3(b)). The flow intensity and thermal convection are of moderate strength with $Re = 130$ and $Pe = 40.9$. The horizontal convection of energy away from the beam impact area 'drives' the trijunction away from the beam impact area, creating a shallow pool with aspect ratio $D_{pool}/d_{pool} = 10.4$.

The aluminum vaporization rate is 0.201 kg h^{-1} (5.59×10^{-5} kg s^{-1}), as calculated from an integration of the mass flux expression (Equation (17)) over the top surface of the pool. The energy balance of Table III shows that only 2.5% of the incident energy is used for vaporization. Large fractions are lost to the water-cooled platform and the formation of skip electrons, whereas a small percentage is lost to thermal radiation. The energy flow balances to 0.1% on mesh M1 and to the indicated precision on mesh M2.
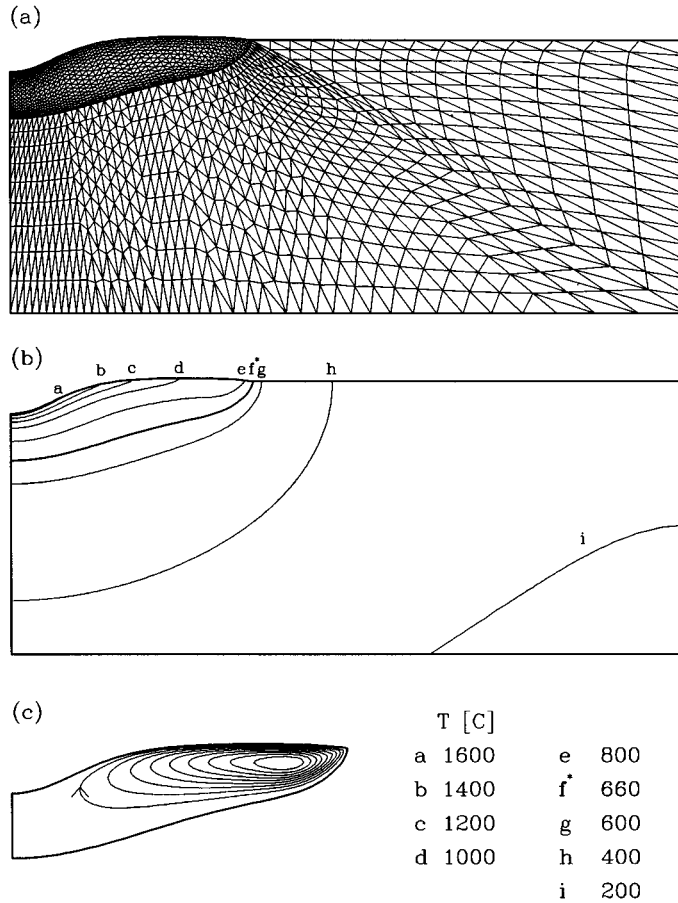
Figure 3. Results for base case (material properties and operating parameters listed in Appendix I and Table II) on mesh M2. (a) Deformed mesh, (b) temperature contours, (c) streamfunction contours.

Table III. Heat-losses as a percentage of incident e-beam power (28 kW) for base case

Contribution	Mesh M1	Mesh M2
Platform	80.0	80.1
Skip	17.0	17.0
Evaporation	2.5	2.5
Thermal radiation	0.4	0.4
Total	99.9	100.0

4.2. Electron-beam power variations

Calculations were performed in which the e-beam power, Q_b, was varied from 24 to 32 kW, with all other parameters and properties at their base case values (see Figure 4). For the condition where $Q_b = 32$ kW, the streamfunction and temperature contours for the solid region are plotted in Figure 4(a). For $Q_b = 24$, 28 and 32 kW, the surface temperature, vapor flux and velocity are plotted versus r in the pool area (see Figure 4(b–d)). Finally, the vaporization rate is plotted versus beam power in Figure 4(e).

The streamlines are smooth, suggesting that the flow field is well resolved (see Figure 4(a)). However, the surface velocity profiles of Figure 4(d) show small spurious oscillations in the region near the trijunction where the liquid is decelerating. When $Q_b = 28$ kW, differences in the curves for the two meshes are visible. These fluctuations are associated with the difficulties in achieving numerical convergence at lower values of the viscosity ratio μ/μ_{meas}. However, all of the pool boundaries, and the temperature and vaporization profiles, are well resolved. Differences between these results for the two meshes are generally very small (see Figure 4(b, c and e)). Since these are often the key variables of interest, the marginal resolution of the flow field can be tolerated.

As the e-beam power is increased from 28 to 32 kW, the diameter of the pool increases by 12.8%, while the depth at the symmetry axis decreases by 3.72% (see Figure 3(a) and 4(a)). Most of the additional 4 kW is transported by convection to the pool boundary near the trijunction, giving an increase in pool diameter with little change in depth.

The surface temperature profile varies little with e-beam power except for the stretch in the lateral direction associated with the increase in pool diameter (see Figure 4(b)). The inflection point near the trijunction is the result of thermal convection. As the surface liquid approaches the trijunction there is a steep decrease in surface temperature. An associated gradient in the surface tension (Marangoni effect) causes a significant local acceleration of surface liquid before it reaches the trijunction (see Figure 4(d)).

As the e-beam power is increased by 33%, from 24 to 32 kW the surface temperature at $r = 0$ increases by only 72°C, while the evaporation flux at this same location increases by 92.9% (see Figure 4(c)). At 1750°C, there is a 2-fold increase in vapor pressure for a 76°C increase in temperature (see Equation (17) and Appendix A). For the condition $24 \leq Q_b \leq 32$ kW, the dependence of the evaporation flux at $r = 0$ and rate on power is nearly linear (see Figure 4(c, e)). The curves for the vapor flux show that most of the metal is evaporated in the beam impact area.

The weak dependence of surface temperature and evaporation rate on beam power indicates the ability of this evaporation system to relieve thermal and mechanical stress. As the beam power is increased, there is an increase in the pool diameter, the circulation rate (see Figure 4d), and the convective transport of energy away from the beam impact area. In addition, the

energy loss associated with evaporation increases, further reducing the temperature increases in the beam impact area. Finally, the increasing thrust of the departing vapor drives the pool down towards the water-cooled platform, decreasing the conduction path length between the beam and the cooling system, which slows the rate of temperature increase.

A linear dependence of the evaporation rate on e-beam power was also obtained in earlier studies of aluminum evaporation from planar melts without Marangoni effects [17–19]. Those results and the calculations of the current study suggest that a linear region may be present for a variety of geometries and operating conditions. It is important to note that the dependence is stronger at lower power. Observing that the evaporation rate curve of Figure 5(e) must pass through the origin, it is apparent that the functional dependence of the evaporation rate must be stronger than linear. At lower power the strong sensitivity of the evaporation rate to temperature becomes more evident as the roles of free boundaries and thermal convection are reduced.
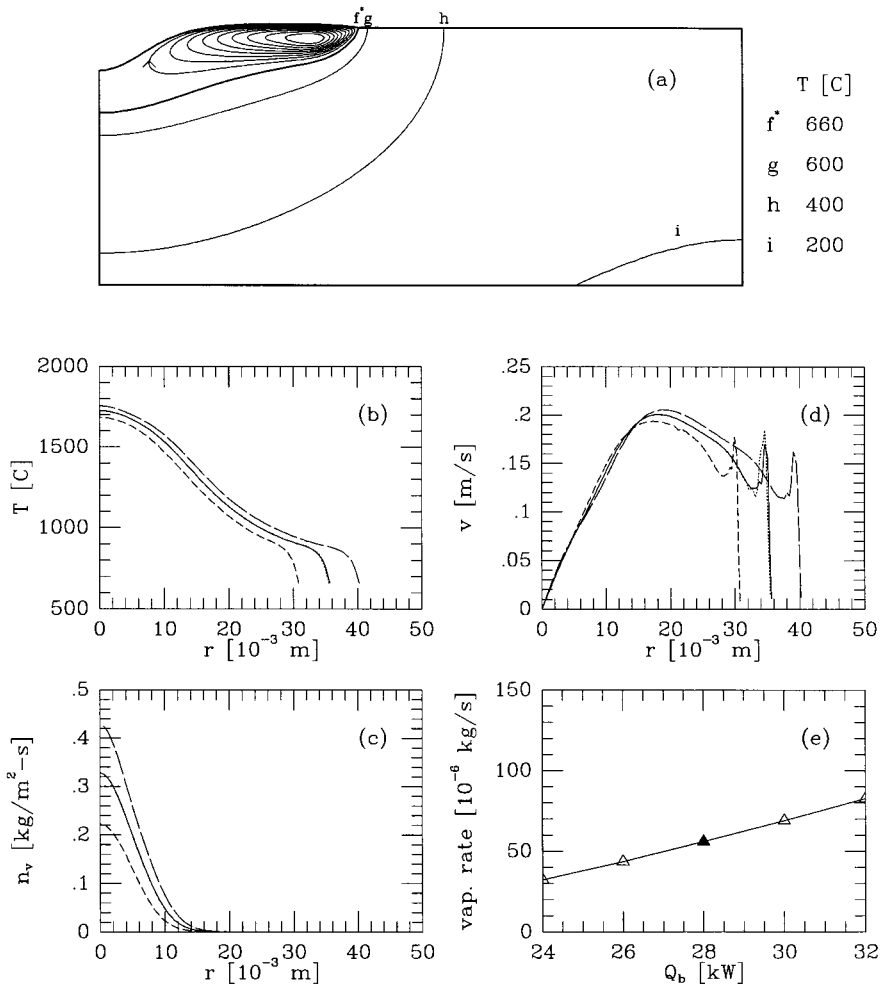
Figure 4. Effects of variations in e-beam power. (a) Streamfunction and temperature contours for $Q_b = 32$ kW. Surface variables in pool area: (b) temperature; (c) vapor flux; (d) velocity for $Q_b = 24$ kW and M2 mesh (- - - -), $Q_b = 28$ kW and M2 mesh (——), $Q_b = 32$ kW and M2 mesh (– –), and $Q_b = 28$ kW and M1 mesh ($\cdot\cdot\cdot$); (e) vaporization rate versus beam power for M1 and M2 meshes (curves coincide to resolution of plot).
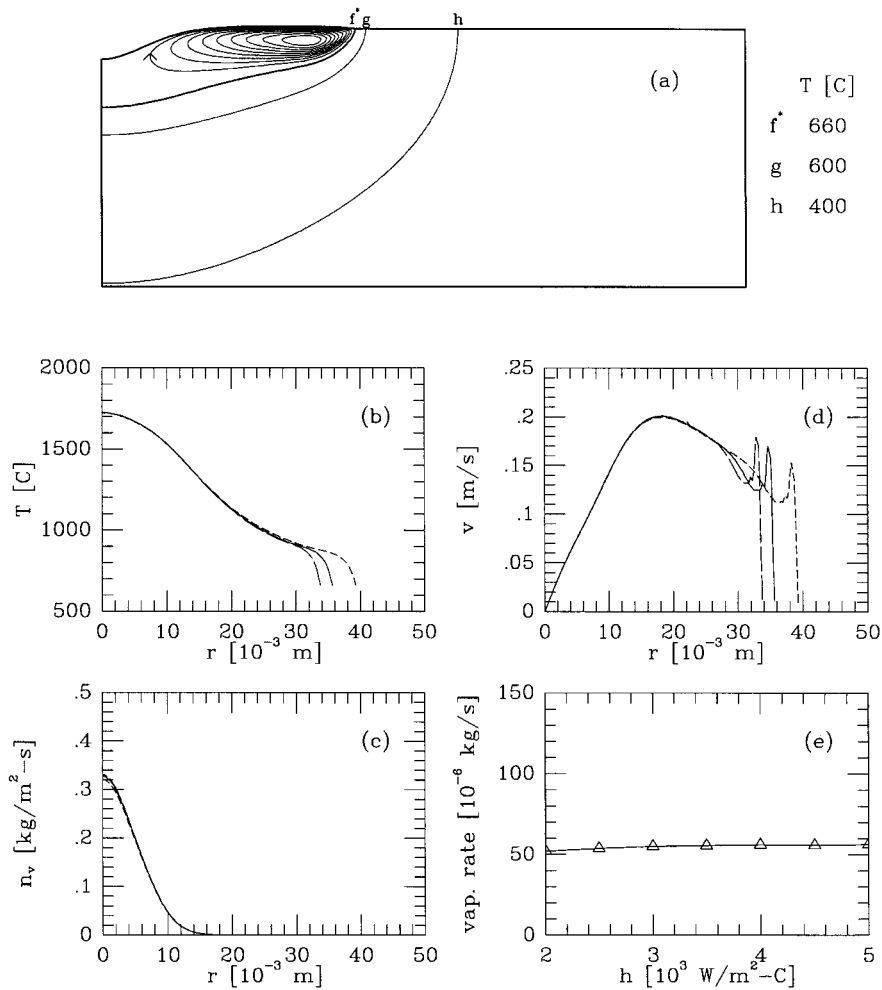
Figure 5. Effects of variations in the platform heat transfer coefficient, h_{pl}. (a) Streamfunction and temperature contours for $h_{pl} = 3$ kW m^{-2} K^{-1}. Surface variables in pool area: (b) temperature; (c) vapor flux; (d) velocity for $h_{pl} = 3$ kW m^{-2} K^{-1} and M2 mesh (- - - -), $h_{pl} = 4$ kW m^{-2} K^{-1} and M2 mesh (——), and $h_{pl} = 5$ kW m^{-2} K^{-1} and M2 mesh (– –); (e) vaporization rate versus platform heat transfer coefficient for M1 and M2 meshes (curves coincide to resolution of plot).

4.3. Variation in heat transfer coefficient

Calculations were performed in which the heat transfer coefficient at the interface between the solid aluminum and the water-cooled platform was varied between 2 and 5 kW m^{-2} K^{-1}. Streamfunction contours and temperature contours in the solid region are shown in Figure 5(a) for $h_{pl} = 3$ kW m^{-2} K^{-1}. Profiles for the surface temperature, evaporation flux and velocity are plotted in Figure 5(b–d) for $h_{pl} = 3$, 4 and 5 kW m^{-2} K^{-1}, respectively. Finally, the evaporation rate versus h_{pl} is plotted in Figure 5(e).

At $h_{pl} = 3$ kW m^{-2} K^{-1}, the streamfunction contours are smooth, but the surface velocity profiles exhibit some spurious oscillations near the trijunction area. The surface profiles for temperature and evaporation flux are well-resolved (see Figure 5(b, c)).

As h_{pl} decreases from 4 to 3 kW m^{-2} K^{-1}, the diameter and depth of the pool increase by 10.3% and 9.27%, respectively (see Figure 3(a) and 5(a)). In the beam impact area, the surface temperature and vapor flux profiles reveal a very weak dependence on h_{pl} (see Figure 5(b, c)).

For a 2.5-fold increase in the heat transfer coefficient, the total evaporation rate increases by 8.44% (see Figure 5(e)). The improved thermal contact with the water-cooled platform is offset by a size reduction in the pool region of high thermal transport and an increase in the size of the solid aluminum region of lower thermal conductance. As was the case for changes in e-beam power, this vaporization system has a remarkable ability to mitigate the effects of changes in conditions at outside boundaries by rearranging the free boundary locations.

5. CONCLUSIONS

A steady state model is developed for an e-beam vaporization system which includes the interaction of interfaces with material and energy flow. Solutions are obtained with a modified Galerkin finite element method, in which meshes structured with pivoting spines deform to track the locations of solid–liquid and liquid–vapor interfaces joined at a trijunction. The discretized equations are arranged in an arrow matrix and solved with the Newton–Raphson method for the flow and temperature fields, and the interface locations.

Simulations were performed for an aluminum vaporization system in which the e-beam power and thermal contact resistance were varied. For the range of powers selected, the dependence of the evaporation rate on e-beam power is nearly linear, despite the strong effect of temperature on the surface evaporation flux. The evaporation rate is nearly independent of contact resistance. The influence of these two variables is reduced by changes in the flow field and the deformation of the solid–liquid and liquid–vapor interfaces. An accurate model of e-beam evaporation of refractory metals must incorporate these effects.

APPENDIX A. MATERIAL PROPERTIES OF ALUMINUM

Property	Melting point value ($T_{mp} = 660°C$)	Reference
$\rho = \rho_0 + (T - T_{mp})\, d\rho/dT$ $\rho_0 = 2370$ kg m^{-3} $d\rho/dT = -2.63 \times 10^{-1}$ kg m^{-3} K^{-1}	2370 kg m^{-3}	Gebhardt *et al.* [26]
$\beta = (1/\rho_0)(-d\rho/dT)$	1.11×10^{-4} K^{-1}	

Property	Melting point value $(T_{mp} = 660°C)$	Reference
$\mu = \mu_1 \exp(E/RT)$ $\quad \mu_1 = 1.492 \times 10^{-4}$ kg m^{-1} s^{-1} $\quad E = 1.65 \times 10^4$ J mole^{-1} $\quad R = 8.314$ J mole^{-1} K^{-1}	1.25×10^{-3} kg m^{-1} s^{-1}	Brandes [27]
$k = k_{mp} + (T - T_{mp})\, dk/dT$ $\quad k_{mp} = 94.0$ W m^{-1} K^{-1} $\quad dk/dT = 3.33 \times 10^{-2}$ W m^{-1} K^{-2}	94.0 W m^{-1} K^{-1}	Brandes [27]
$C_p = 1180$ J kg^{-1} K^{-1}	1180 J kg^{-1} K^{-1}	Chase *et al.* [28]
$k_s = k_{mp} + (T - T_{mp})\, dk/dT$ $\quad k_{mp} = 197$ W m^{-1} K^{-1} $\quad dk/dT = -6.39 \times 10^{-2}$ W m^{-1} K^{-2}	197 W m^{-1} K^{-1}	Touloukian *et al.* [29]
$\sigma = \sigma_{mp} + (T - T_{mp})\, d\sigma/dT$ $\quad \sigma_{mp} = 0.865$ N m^{-1} $\quad d\sigma/dT = -1.2 \times 10^{-4}$ N m^{-1} K^{-1}	0.865 N m^{-1}	Gourmiri *et al.* [30]
$p_{vap} = p_1 \exp(E/RT)$ $\quad p_1 = 8.25 \times 10^{10}$ N m^{-2} $\quad E = -3.10 \times 10^5$ J mole^{-1}	3.63×10^{-7} N m^{-2}	Alcock *et al.* [31]
$\Delta H_{vap} = (R/M)\, d\ln(p_{vap})/d(1/T)$	1.15×10^7 J kg^{-1}	
$\varepsilon = a_1(rT)^{1/2} - a_2 rT$	0.0826	M.A. Havstad, private communication, 1988
$\quad a_1 = 5.76\ (\Omega\ \text{m K})^{1/2}$ $\quad a_2 = 12.4\ \Omega$ m K $\quad r = 2.35 \times 10^{-7}\ \Omega$ m		Miller [32]
$\gamma = 0.83$	0.83	Schiller *et al.* [2]

APPENDIX B. NOMENCLATURE

$c_k,\ c_k'$	constants, Equations (23), (24)
C_p	heat capacity
D_{pool}	melt pool diameter
d_{pool}	melt pool depth at $r = 0$
$\underline{g}$	gravitational acceleration vector
$\bar{h}$	local interface elevation
$\bar{h}_0$	average elevation of metal in disk
h_1	average elevation of metal in pool
h_s	elevation of solid
h_{pl}	platform heat transfer coefficient
ΔH_{vap}	heat of vaporization

k	thermal conductivity
L_c	capillary length
M	molecular weight
$\underline{M}$	surface force balance
$\underline{n}$	unit normal vector
n_v	evaporative mass flux
p	pressure
Pe	Peclet number
p_{vap}	vapor pressure
$\underline{q}$	heat flux vector
q_b	electron-beam heat flux
q_r	radiative heat flux
q_v	evaporative heat flux
Q_b	electron-beam power
r_{disk}	disk radius
R	gas constant
Re	Reynolds number
s	arc-length in r–z plane
s_1	arc-length out of r–z plane
$\underline{t}$	unit tangent vector in r–z plane
$\underline{t}_1$	unit tangent vector out of r–z plane
T	temperature
T_{mp}	melting point
$\underline{u}$	fluid velocity vector
u_{max}	maximum fluid velocity
r, z	co-ordinates

Greek letters

α	thermal diffusivity
β	volume expansion coefficient
γ	skip coefficient
$\underline{\underline{\delta}}$	unit tensor
$\underline{\delta}_r, \underline{\delta}_z$	unit vector in co-ordinate direction
ε	emissivity
μ	viscosity
π_v	vapor thrust
ρ	density
$\rho_1, \theta, \rho_2, \rho'$	spine variables
σ	surface tension
σ_b	Gaussian beam radius
σ_{SB}	Stefan–Boltzman constant
$\underline{\underline{\tau}}$	stress tensor

Subscripts

0	reference state
l	liquid phase
lv	liquid–vapor interface
s	solid phase

sl	solid–liquid interface
tri	trijunction
w	wall quantity
∞	surroundings

REFERENCES

1. R.J. Hill, *Physical Vapor Deposition*, BOC group, Inc., 1986.
2. S. Schiller, U. Heisig and S. Panzer, *Electron Beam Technology*, Wiley, New York, 1982.
3. M.A. McClelland, 'Application of streamwise diffusion to time-dependent free convection of liquid metals', *Int. J. Numer. Methods Fluids*, **19**, 1061–1071 (1994).
4. M.A. McClelland, 'Time-dependent liquid metal flows with free convection and a deformable free surface', *Int. J. Numer. Methods Fluids*, **20**, 603–620 (1995).
5. H.S. Kheshgi and P.M. Gresho, 'Analysis of electron-beam vaporization of refractory metals', in R. Bakish (ed.), *Electron Beam Melting and Refining State of the Art 1986*, Bakish Materials Corp., Englewood, NJ, 1986, pp. 68–79.
6. A. Służalec, 'Flow of metal undergoing laser irradiation', *Numer. Heat Transfer*, **13**, 256–263 (1988).
7. T. Zacharia, A.H. Eraslan, D.K. Aidun and S.A. David, 'Three-dimensional transient model for arc welding process', *Metall. Trans. B*, **20B**, 645–659 (1989).
8. T. Zacharia, S.A. David, J.M. Vitek and H.G. Kraus, 'Computational modeling of stationary gas- tungsten-arc weld pools and comparison to stainless steel 304 experimental results', *Metall. Trans. B*, **22B**, 243–257 (1991).
9. T. Zacharia, S.A. David and J.M. Vitek, 'Understanding heat and fluid flow in linear GTA welds', in S.A. David and J.M. Vitek (eds.), *International Trends in Welding Science and Technology*, ASM International, Ohio, 1992, volume 3, pp. 27–31.
10. K. Ravindran, J. Srinivasan and A.G. Marathe, 'Finite element study on the role of convection in laser surface melting', *Numer. Heat Transfer, Part A*, **26**, 601–618 (1994).
11. P.A. Sackinger, R.A. Brown and J.J. Derby, 'A finite element method for the analysis of fluid flow, heat transfer and free interfaces in Czochralski crystal growth', *Int. J. Numer. Methods Fluids*, **9**, 453–492 (1989).
12. R.A. Brown, T.A. Kinney, P.A. Sackinger and D.E. Bornside, 'Toward an integrated analysis of czochralski growth', *J. Crystal Growth*, **97**, 99–115 (1989).
13. S.F. Kistler and L.E. Scriven, 'Coating flows', in J.R.A. Pearson and S.M. Richardson (eds.), *Computational analysis of polymer processing*, Applied Science Publishers, London, 1983, pp. 243–299.
14. M.C. Tsai and S. Kou, 'Marangoni convection in weld pools with a free surface', *Int. J. Numer. Methods Fluids*, **9**, 1503–1516 (1989).
15. G.W. Lan and S. Kou, 'Heat transfer, fluid flow and interface shapes in floating zone crystal growth', *J. Crystal Growth*, **108**, 351–366 (1991).
16. G.W. Lan and S. Kou, 'Radial dopant segregation in zero-gravity floating-zone crystal growth', *J. Crystal Growth*, **132**, 578–591 (1993).
17. K.W. Westerberg, M.A. McClelland and B.A. Finlayson, 'The tracking of interfaces in an electron-beam vaporizer', in R.W. Lewis (ed.), *Numerical Methods in Thermal Problems*, Pineridge Press, Swansea, 1993, volume VIII, Pt. 2, pp. 1322–1333.
18. K.W. Westerberg, M.A. McClelland and B.A. Finlayson, 'Numerical simulation of material and energy flow in an e-beam melt furnace', in R. Bakish (ed.), *Electron Beam Melting and Refining State of the Art 1993*, Bakish Materials Corp., Englewood, NJ, 1993, pp. 153–165.
19. K.W. Westerberg, M.A. McClelland and B.A. Finlayson, 'The interaction of flow, heat transfer, and free interfaces in an electron-beam vaporization system for metals', *Paper 124e*, 1994 Annual AIChE Meeting, San Francisco, CA, 1994.
20. T. Tran Cong and G.A. Bird, 'One-dimensional outgassing problem', *Phys. Fluids*, **21**, 327–333 (1978).
21. O.C. Zienkiewicz, *The Finite Element Method*, McGraw-Hill, London, 3rd edition, 1977.
22. K.W. Westerberg, 'A finite element method for flow problems with free surfaces and moving fronts', *Ph.D. Thesis*, University of Washington, 1992.
23. K.W. Westerberg, C. Wiklof and B.A. Finlayson, 'Time-dependent finite element models of phase-change problems with moving heat sources', *Numer. Heat Transfer, Part B*, **25**, 119–143 (1994).
24. P. Hood, 'Frontal solution program for unsymmetric matrices', *Int. J. Numer. Methods Engn.*, **10**, 379–399 (1976).
25. R.S. Ransing, Y. Zheng and R.W. Lewis, 'Potential applications of intelligent preprocessing in the numerical simulation of castings', in R.W. Lewis (ed.), *Numerical Methods in Thermal Problems*, volume VIII, Pt. 2, Pineridge Press, Swansea, 1993, pp. 361–375.

26. E. Gephardt, M. Becker and S. Dorner, *Aluminum*, **31**, 315 (1955).
27. E.A. Brandes, *Smithelle's Metals Reference Book*, Butterworths, Guildford, UK, 6th edition, 1983.
28. M.W. Chase, C.A. Davies, J.R. Downey, D.J. Frurip, R.A. McDonald and A.N. Syverud, 'JANAF thermochemical tables', *J. Phys. Chem. Ref. Data*, **14**, 61–64 (1985).
29. Y.S. Touloukian, R.W. Powell, C.Y. Ho and P.G. Klemens, 'Thermal conductivity', *Metallic Elements and Alloys Thermophysical Properties of Matter*, **1**, 1–9 (1970).
30. L. Gourmiri, J.C. Joud and P. Desre, 'Tensions superficielles d'alliages liquides binaires presentant un caractere d'immiscibilite: Al–Pb, Al–Bi, Al–Sn et Zn–Bi', *Surface Science*, **83**, 471–486 (1979).
31. C.B. Alcock, V.P. Itkin and M.K. Horrigan, 'Vapour pressure equations for the metallic elements: 298–2500 K', *Canadian Metallurgical Quarterly*, **23**, 309–313 (1984).
32. J.C. Miller, 'Optical properties of liquid metals at high temperatures', *Phil. Mag.*, **20**, 1115–1132 (1969).